metals

Article

A Comparative Study of Acicular Ferrite Transformation Behavior between Surface and Interior in a Low C–Mn Steel by HT-LSCM

Xiaojin Liu [1], Guo Yuan [1,*], Raja. Devesh Kumar Misra [2] and Guodong Wang [1]

[1] The State Key Laboratory of Rolling and Automation, Northeastern University, Shenyang 110819, China; liuxiaojn@126.com (X.L.); wanggdneu@163.com (G.W.)
[2] Laboratory for Excellence in Advanced Steel Research, Department of Metallurgical, Materials and Biomedical Engineering, University of Texas at El Paso, El Paso, TX 79968, USA; dmisra2@utep.edu
* Correspondence: yuanguo@ral.neu.edu.cn; Tel.: +86-024-83687220

Abstract: In this study, the acicular ferrite transformation behavior of a Ti–Ca deoxidized low carbon steel was studied using a high-temperature laser scanning confocal microscopy (HT-LSCM). The in situ observation of the transformation behavior on the sample surface with different cooling rates was achieved by HT-LSCM. The microstructure between the surface and interior of the HT-LSCM sample was compared. The results showed that Ti–Ca oxide particles were effective sites for acicular ferrite (AF) nucleation. The start transformation temperature at grain boundaries and intragranular particles decreased with an increase in cooling rate, but the AF nucleation rate increased and the surface microstructure was more interlocked. The sample surface microstructure obtained at 3 °C/s was dominated by ferrite side plates, while the ferrite nucleating sites transferred from grain boundaries to intragranular particles when the cooling rate was 15 °C/s. Moreover, it was interesting that the microstructure and microhardness of the sample surface and interior were different. The AF dominating microstructure, obtained in the sample interior, was much finer than the sample surface, and the microhardness of the sample surface was much lower than the sample interior. The combined factors led to a coarse size of AF on the sample surface. AF formed at a higher temperature resulted in the coarse size. The available particles for AF nucleation on the sample surface were quite limited, such that hard impingement between AF plates was much weaker than that in the sample interior. In addition, the transformation stress in austenite on the sample surface could be largely released, which contributed to a coarser AF plate size. The coarse grain size, low dislocation concentration and low carbon content led to lower hardness on the sample surface.

Keywords: low carbon steel; Ti–Ca deoxidation; transformation behavior; in situ observation; acicular ferrite

check for updates

Citation: Liu, X.; Yuan, G.; Misra, R..D.K.; Wang, G. A Comparative Study of Acicular Ferrite Transformation Behavior between Surface and Interior in a Low C–Mn Steel by HT-LSCM. *Metals* **2021**, *11*, 699. https://doi.org/10.3390/met11050699

Academic Editor: Marcello Cabibbo

Received: 23 March 2021
Accepted: 22 April 2021
Published: 24 April 2021

1. Introduction

The acicular ferrite formed in steel can be used in the technology called oxides metallurgy, where the acicular ferrite can nucleate at the surface of oxide inclusion during the transformation from austenite to ferrite. It is well known that the formation of acicular ferrite is strictly influenced by inclusion type, prior austenite grain size and cooling rate [1,2]. Intragranular acicular ferrite (AF) is known to provide an optimal combination of high strength and good toughness, because of its refined structure with high-angle grain boundaries and high-density of dislocations [3,4]. Thus, the fine interlocking microstructure is known to improve toughness in both the heat-affected zone (HAZ) or weld metal, and the deoxidized high-strength low-alloy (HSLA) steel [3,5–7].

High-temperature laser scanning confocal microscopy (HT-LSCM) has been widely used to study the phase transformation from austenite to ferrite and grain growth in steels [8–11]. HT-LSCM is also an effective method to study inclusion-induced AF. Hanamura et al. [12] used this method to observe the nucleation of AF around inclusions and confirmed the thermodynamic calculation results by in situ observation in 1999. Thereafter, Kikuchi et al. used HT-LSCM to investigate the microstructure refinement and deoxidation inclusions in low-carbon high-manganese steels through Ti deoxidation [13–15]. Loder et al. and Wen et al. reported in situ observations of AF formation in steels containing complex oxides [9,16]. Zhang et al. explored the formation of intragranular AF in C–Mn steel with different chemical compositions, austenite grain size and characteristics of inclusion using HT-LSCM [17]. Wan and coworkers observed and investigated grain refinement of HAZ in HSLA steels containing effective inclusion particles, [10,18]. Mu et al. discussed the effects of the cooling rate, grain size, and inclusion composition on the ferrite fraction and phase-transition temperature [8,19]. Wang et al. studied the nucleation and growth of AF at different cooling rates in Ti-Ca-Zr deoxidized low-carbon steel [20]. Zou et al. explored the nucleation and growth of ferrite laths in the HAZ of EH36-Mg shipbuilding steel subjected to different heat inputs [21]. Moreover, intragranular ferrite growth kinetics was systematically analyzed by in situ methodology [22].

HT-LSCM is an advantageous method for the direct study of AF transformation behavior. However, the results of HT-LSCM observations could only reflect the AF transition on the surface of the HT-LSCM sample. The microstructure may be different between the surface and interior of the HT-LSCM sample. So far, no such research has been carried out according to the present literature. In order to clarify the difference between the in situ observation of the sample surface and the phase transition in the sample interior, and to better understand the AF phase transformation mechanism, the microstructure between the surface and interior of the HT-LSCM sample, in a low C–Mn steel with effective inclusions at different cooling rates, were characterized and analyzed.

2. Materials and Methods

Ti oxide showed distinct AF nucleating ability and received extensive research. In addition, strong deoxidants such as Ca, Mg and Zr are usually added together with Ti to achieve a dispersed distribution of fine-sized oxide. In the present research, low C–Mn steel with Ti–Ca complex deoxidation was chosen for the inclusion-induced AF transformation study. The experimental steel was melted in a 10 kg laboratory vacuum induction furnace. Ti-Ca was added as FeTi30 and SiCa30 alloy into the steel liquid before casting. The steel composition was shown in Table 1. Samples were taken from the cast ingot for microstructure observation and inclusion analysis by a DM2500 M optical microscope (OM, Leica Microsystems, Wetzlar, Germany) and an Ultra-55 scanning electron microscope (SEM, Carl Zeiss, Jena, Germany).

Table 1. Chemical composition of the experimental steel, wt.%.

C	Si	Mn	Ti	Ca	P	S	Fe
0.08	0.25	1.56	0.01	0.001	0.011	0.007	Bal.

The cast ingot was hot rolled into the steel plate and used for the subsequent experiment. Round samples with a diameter of 6 mm and thickness of 3 mm were machined and the top flat surface was mirror polished. The in situ observation was carried out on a LSM 510 Zeiss high-temperature laser scanning confocal microscope (LSCM, Carl Zeiss, Jena, Germany). The samples were heated to 1300 °C and held for 1 min, then cooled to room temperature with cooling rates of 3 °C/s, 6 °C/s and 15 °C/s, respectively. Transformation behaviors on the top surface were recorded by the microscope. Afterwards, the sample surface microstructures were observed before and after 4% nital etching. Furthermore, the samples were cut in half as shown in Figure 1 and the matrix microstructures inside the samples were also characterized by OM and electron backscattered diffraction (EBSD, Hikari, EDAX-TSL, Draper, UT, USA). The characterization position was at the center as circled in Figure 1. The macro Vickers hardness values for the top surface and inside the sample were measured by a KB hardness testing machine (KB Prüftechnik, Hochdorf-

Assenheim, Germany). The microhardness was tested by an FM-700 microhardness tester (FUTURE-TECH CORP., Kawasaki, Japan). For comparison, the transformation-dilation experiment was carried out on Formastor-FII full-automatic transformation equipment (Fuji Electronic, Tokyo, Japan) using cylinder samples of dimensions Φ3 mm × 10 mm. The thermal cycles were similar to that for LSCM.

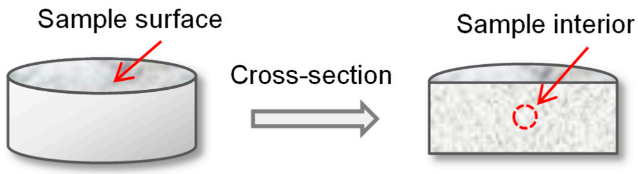

Figure 1. Schematic diagram of microstructural characterization positions of LSCM samples.

3. Results and Discussion

3.1. As-Cast Microstructure and Inclusion

The liquid steel was solidified in a copper mold and then taken out for cooling in air. A sample was prepared from the upper part of the ingot and the optical microstructure was shown in Figure 2. The morphology was of an AF-dominating type. The prior austenite grain size was extremely large in the cast condition and the whole field of view in Figure 2 was even within one parent austenite grain. Coarse ferrite plates forming at higher temperatures extended to a long distance and divided the austenite grain into parts. Finer ferrite plates formed within the local regions during cooling.

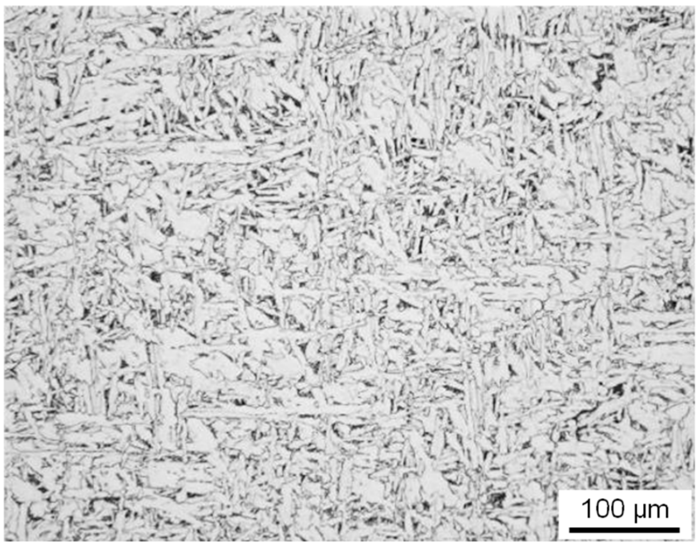

Figure 2. Optical microstructure of the as-cast steel.

The effective inclusion-inducing AF nucleation was characterized by SEM as shown in Figure 3. The Ti-Ca oxide inclusion also contained Al-Ca-Mn-S elements. Several mechanisms for inclusion-induced ferrite nucleation have been proposed including inert substrate mechanism, thermal strain mechanism, element depletion mechanism and lattice matching mechanism [23,24]. For Ti-oxide, most research believed the Mn depletion zone (MDZ) mechanism was reasonable, which was formed by Mn absorption into Ti-oxide particles or MnS adhering precipitation [1]. The formation of MDZ caused a decrease in Mn content and an increase in transformation temperature, which promoted intragranular AF nucleation around the inclusion [25,26]. In addition, the driving force for ferrite formation, i.e., the Gibbs free energy change for $\gamma \rightarrow \alpha$, increased with a decrease in Mn content, which contributed to promoting AF nucleation [27]. In the present experimental steel, Ti oxide was the main inclusion type and was considered to be effective through the MDZ mechanism.

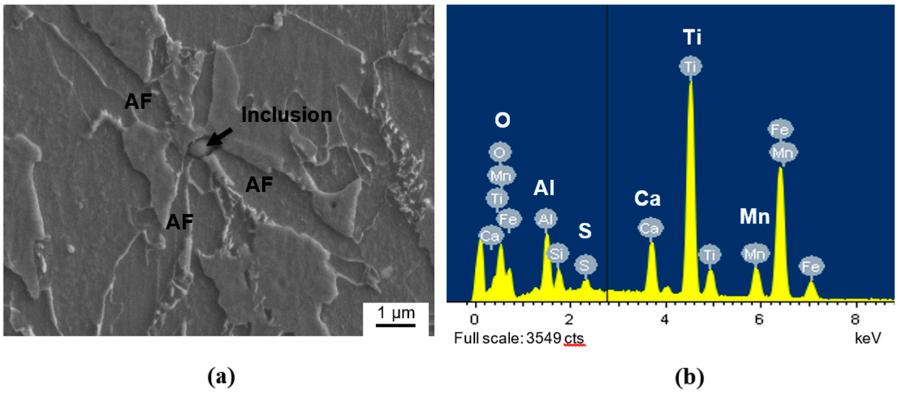

Figure 3. (**a**) SEM micrograph of the as-cast steel and (**b**) EDS analysis of the inclusion in (**a**).

3.2. In Situ Transformation Behaviors by LSCM

The whole transformation processes during cooling at different cooling rates were recorded by LSCM and the typical micrographs were presented in Figures 4–6. LSCM presented the sample surface change and temperature simultaneously so that we could identify the start temperatures of transformation at grain boundaries or at intragranular particles. Austenitizing temperature was chosen as 1300 °C to acquire a large enough austenite grain size for promoting intragranular ferrite formation. At 3 °C/s, transformation started at 680 °C and ferrite nucleation first happened on austenite grain boundaries, as indicated in Figure 4a. The initial growth of the grain boundary ferrite (GBF) was relatively slow. As the GBF grew along the boundaries and then towards the interior, intragranular ferrite plates were found to nucleate at 632 °C, as shown in Figure 4b. The subsequent transformation was accelerated through two nucleation ways, i.e., from intragranular sites and on boundaries. However, the final microstructure was dominated by the ferrite side plates (FSP) forming from boundaries. Figure 4c showed the intermediate stage of the transforming process. Figure 4d showed the end of transformation at about 575 °C. The coarse ferrite sheaves growing across the whole austenite grain were obvious.

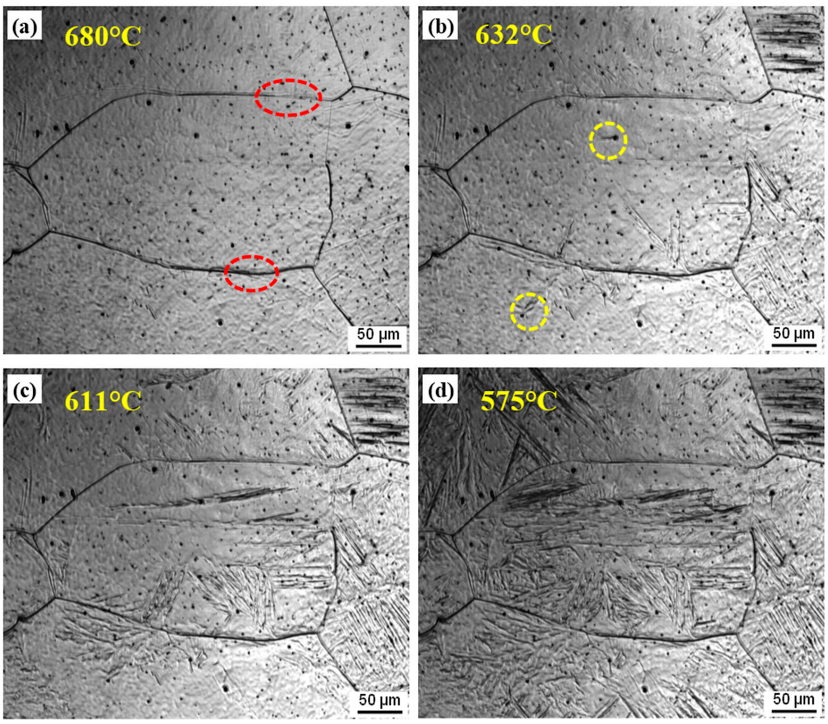

Figure 4. Micrographs by LSCM showing transformation behaviors during cooling at 3 °C/s. The micrographs are taken at (**a**) 680 °C, (**b**) 632 °C, (**c**) 611 °C and (**d**) 575 °C, respectively.

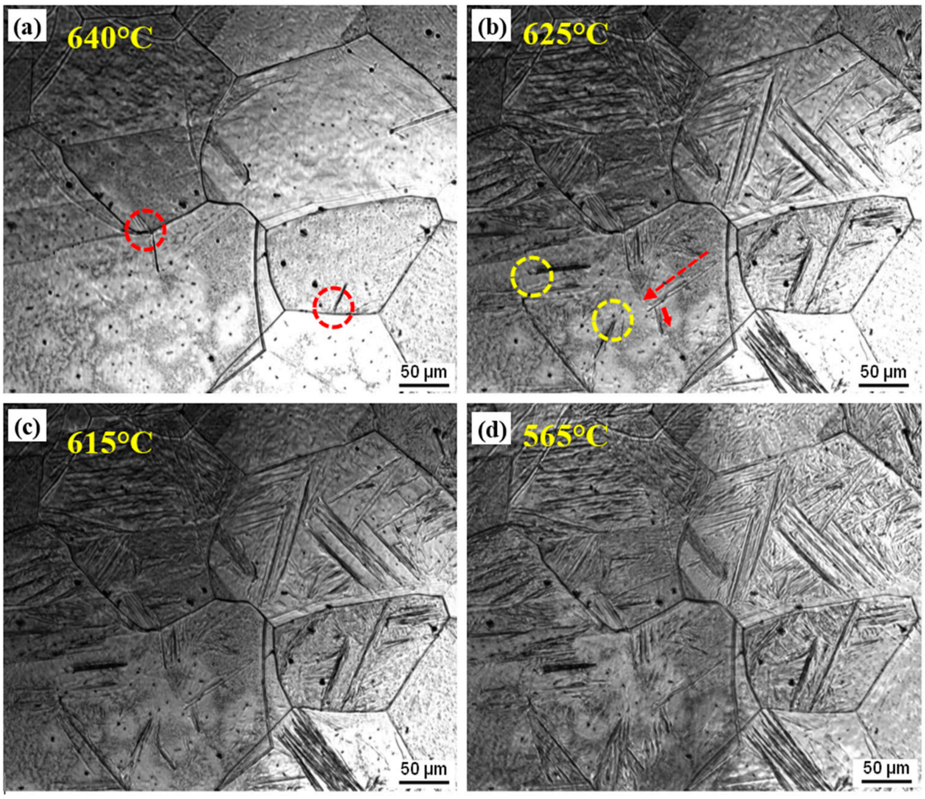

Figure 5. Micrographs by LSCM showing transformation behaviors during cooling at 6 °C/s. The micrographs are taken at (**a**) 640 °C, (**b**) 625 °C, (**c**) 615 °C and (**d**) 565 °C, respectively.

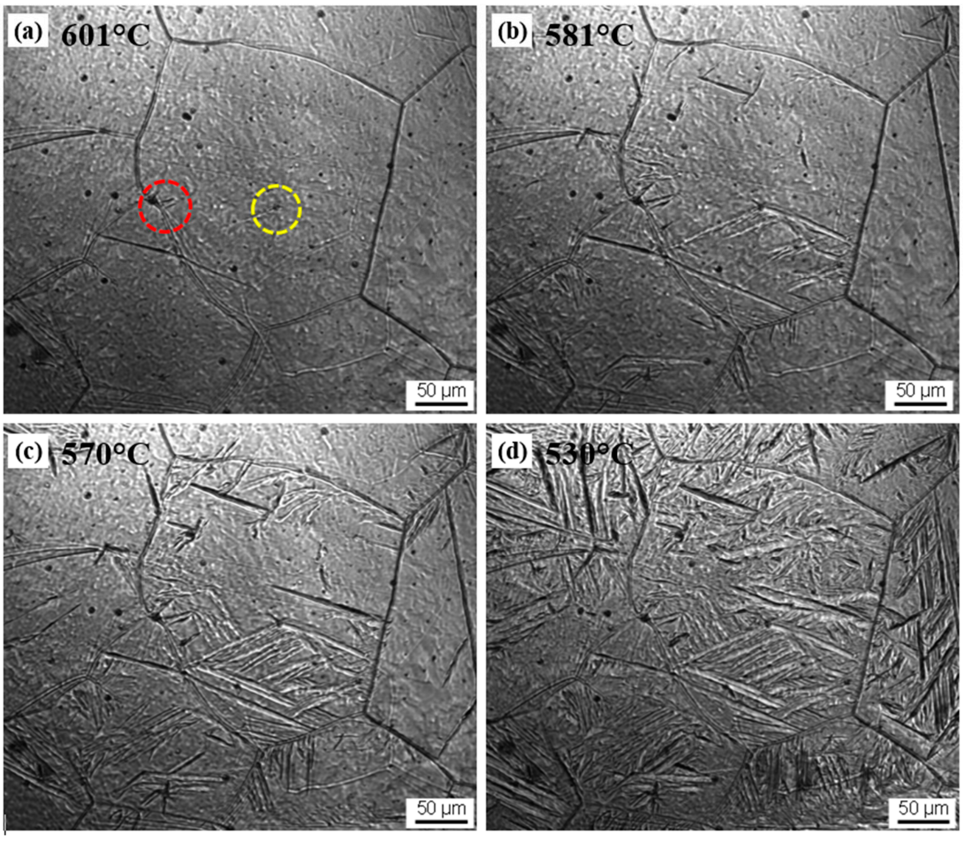

Figure 6. Micrographs by LSCM showing transformation behaviors during cooling at 15 °C/s. The micrographs are taken at (**a**) 601 °C, (**b**) 581 °C, (**c**) 570 °C and (**d**) 530 °C, respectively.

For the cooling rate of 6 °C/s, microstructural evolution was shown in Figure 5. Ferrite nucleation still started from austenite grain boundaries while the start temperature decreased to 670 °C. FSP had grown to a short distance at 640 °C while no intragranular nucleation was observed, as shown in Figure 5a. With the temperature decreasing to 625 °C, a number of intragranular acicular ferrite plates were observed to form, mostly at the intragranular particles. In comparison with Figure 4, the intragranular nucleating rate became higher and the AF fraction increased. AF plates were encountered during the growth of FSP, such that the chance for the formation of ferrite sheaves across the whole austenite grain decreased. In addition, the ferrite plates could also originate from the first-formed ferrite plate but with a different orientation, as shown in Figure 5b, where the long red arrow indicated the primary ferrite plate as well as its growth direction, while the short red arrows indicated the secondary ferrite plates. The transformation continued at 615 °C in Figure 5c. The transformation nearly finished at 565 °C, as shown in Figure 5d, and the morphology seemed more interlocked than that for 3 °C/s.

The transformation behavior for the cooling rate of 15 °C/s showed remarkable difference from that of 3 °C/s and 6 °C/s. Ferrite nucleation was observed to start at 601 °C at grain boundaries and intragranular particles simultaneously, as shown in Figure 6a. With the decrease in temperature, in Figure 6b, more intragranular primary and secondary AF plates nucleated and lengthened without the obvious formation of grain boundary FSP. In this condition, the parent austenite grain was segmented into smaller parts by intragranular ferrite plates, see Figure 6c. The AF plates grew in some particular orientations as a result of the K-S orientation relationship with parent austenite and formed a weaving configuration [28,29]. However, this trend did not continue to the end of transformation of all the retained austenite. It seemed that the available intragranular nucleation sites were limited. The AF formation stopped after all the available nucleation sites were used up, which was followed by the formation of parallel ferrite packets between the prior AF plates. Figure 6d showed the finish point of transformation by in situ observation. Even so, the surface microstructure evolution exhibited significant difference from the interior of the sample, which will be revealed in the following section.

3.3. Microstructural Comparison between the Surface and Interior

The optical microstructures of different sample surfaces without etching after LSCM thermal cycles were presented in Figure 7, where two samples with lower austenitizing temperatures of 1000 °C and 1200 °C were also included. The nital etched surface microstructures and corresponding interior microstructures were shown in Figure 8. With a low austenitizing temperature of 1000 °C, the austenite grain size was fine and polygonal ferrite was formed via the reconstructive transformation mechanism, as shown in Figure 7a. With the increase in austenitizing temperature and austenite grain size, the amount of parallel ferrite plates increased and the surface relief phenomenon appeared as a result of the displacive transformation, as shown in Figure 7b,c. For the cooling rate of 15 °C/s (Figure 7d), with the massive formation of intragranular AF, the surface relief also became much clearer.

Figure 8 showed the great difference between the surface and interior microstructures. In general, the interior microstructures for the experimental conditions were significantly finer than the surface. In Figure 8a–c, with the increase in cooling rate, the amount of intragranular AF plates increased and segmented the parent austenite grain into smaller regions. It corresponded to the result of in situ observation by LSCM. For the experimental cooling rates, AF dominating microstructures were always obtained in the interiors of different samples. AF plates obtained at 3 °C/s were coarse (Figure 8a′) and they became much finer as the cooling rate increased to 6 °C/s and 15 °C/s. It was shown from the in situ transformation behavior that the intragranular AF nucleation rate increased at a higher cooling rate and the lengthening of the AF plates also speeded up. On the sample surface, the number of nucleating sites, i.e., effective oxide particles, was limited and the hard impingement probability between AF plates was low such that the AF plates on the sample surface could grow to a large size, but with a small plate number. On the contrary, the AF nucleation rate and hard impingement were remarkably improved in the sample interior and there was less space for AF plates to coarsen, which resulted in much finer microstructure.

The surface and interior microstructures were further analyzed by EBSD with the results shown in Figure 9. For the surface microstructures, the coarse plates and sheaves were characterized by high-angled boundaries. In addition, the low-angled boundary concentration increased with the increase of cooling rate. The interior AF microstructures exhibited dense high-angled boundaries. The AF plates within one parent austenite grain showed some particular orientations as a result of the orientation relationship. In the sample interior, besides the dominating AF plates, there also existed a certain amount of small ferrite grains with granular or quasi-polygonal morphology. It could be distinguished in optical micrographs in Figure 8 and also in EBSD maps. Some research indicated that polygonal ferrite could form from the remaining austenite between acicular ferrite grains, by a reconstructive mechanism after the reaction stasis of acicular ferrite [30]. However, according to the present in situ observation of the continuous cooling transformation behavior, especially for the cooling rates of 6 °C/s and 15 °C/s, austenite could almost completely transform into ferrite plates and packets via a displacive transformation regime accompanied with surface relief. In addition, in the EBSD maps of sample interior, the small granular ferrite grains within one parent austenite grain mostly have one similar or a few particular crystallographic orientations, whereas the orientations of ferrite grains formed by reconstructive mechanism should distribute randomly. This means the granular ferrite grains were actually the transverse sections of AF laths. Their nucleation sites were at inclusions above or beneath the viewing plane. Their formation belonged to the same transforming stage as the acicular ferrite plates.

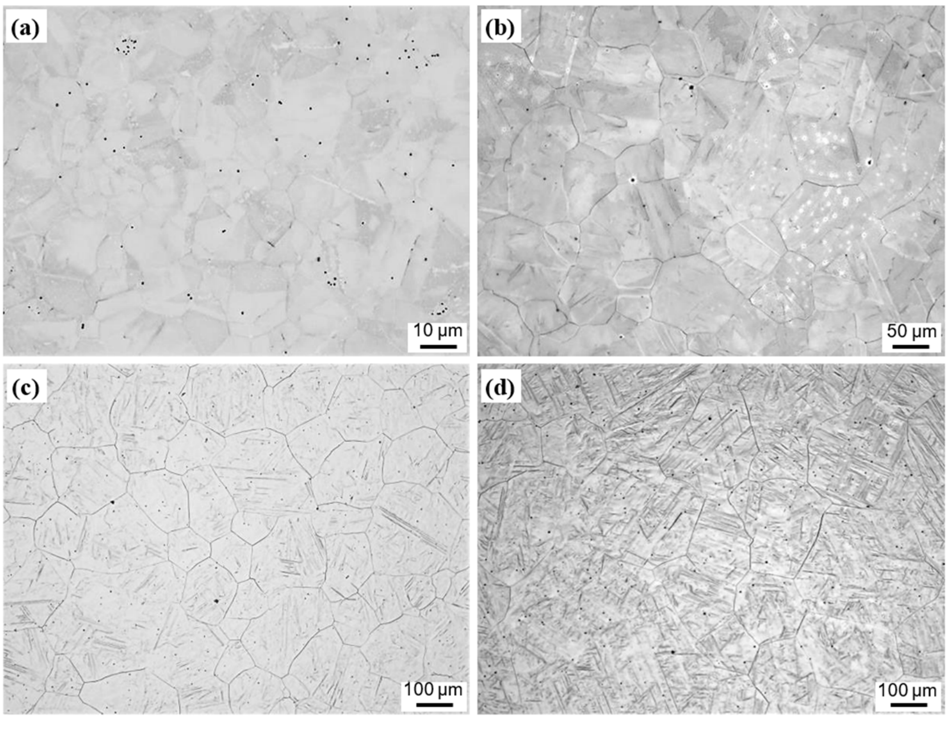

Figure 7. Surface optical micrographs without etching of the samples after LSCM thermal cycles. The austenitizing temperatures and cooling rates are (**a**) 1000 °C–3 °C/s, (**b**) 1200 °C–3 °C/s, (**c**) 1300 °C–3 °C/s and (**d**) 1300 °C–15 °C/s.

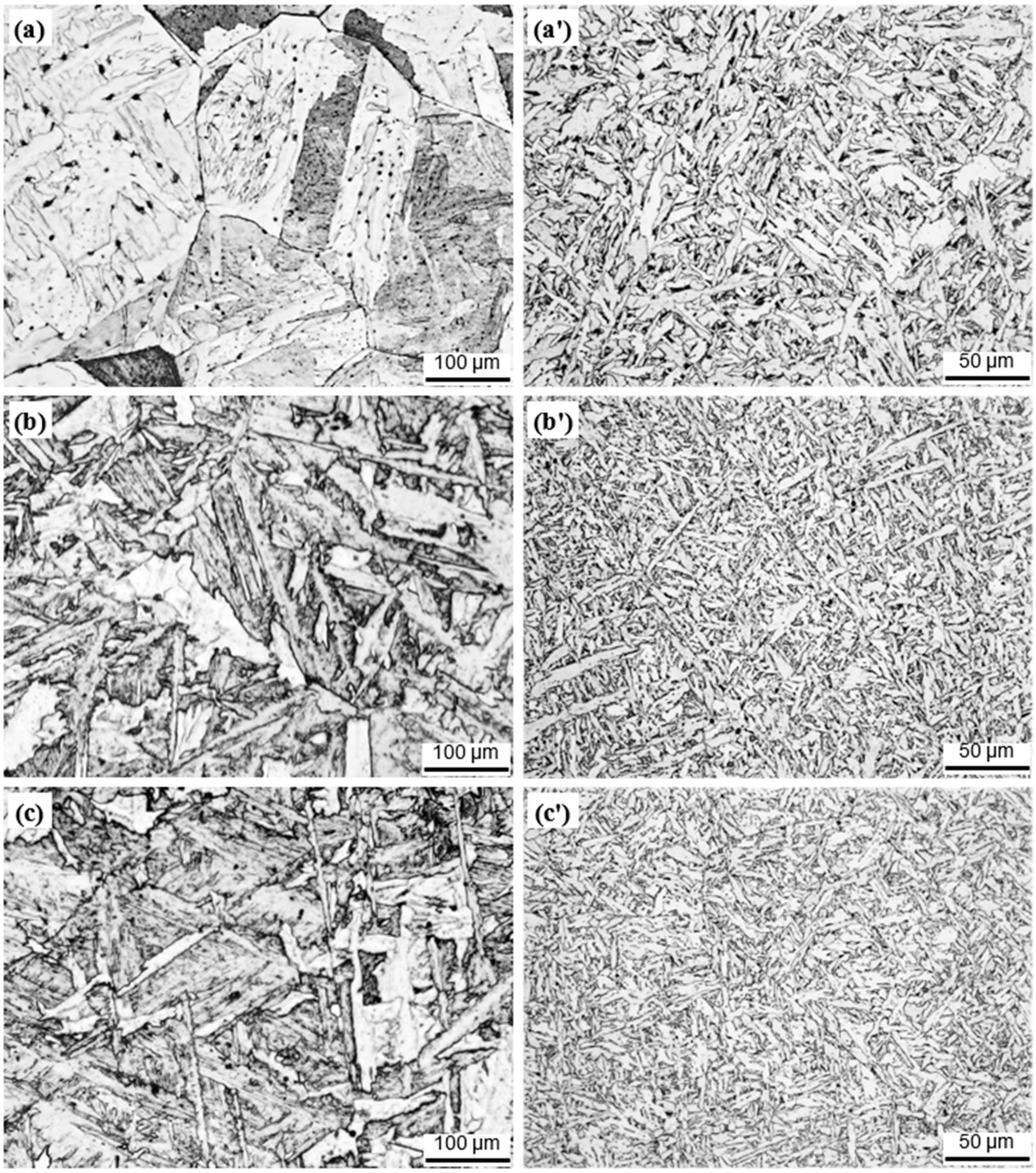

Figure 8. Optical microstructures with nital etching after LSCM thermal cycles. (**a**–**c**) are surface microstructures; (**a′**–**c′**) are interior microstructures; (**a**,**a′**), (**b**,**b′**) and (**c**,**c′**) correspond to cooling rates of 3 °C/s, 6 °C/s and 15 °C/s, respectively.

3.4. Micro and Macrohardness

The micro and macro Vickers hardness values of different microstructures, on the surface and inside the sample obtained under experimental cooling rates, were tested. The results were shown in Figure 10. In Figure 10a, microhardness for both the inside and surface of the sample increased with the increase in cooling rate while the surface microhardness was much lower than the sample interior. In Figure 10b, the macrohardness also increased with the cooling rate, but the difference between the surface and the inside was not obvious. In addition, the micro and macrohardness values tested from the sample interior were consistent with each other. However, the micro and macrohardness values tested from the sample surface varied significantly, where the surface microhardness was much lower than its macrohardness. This result was analyzed combined with microstructures.

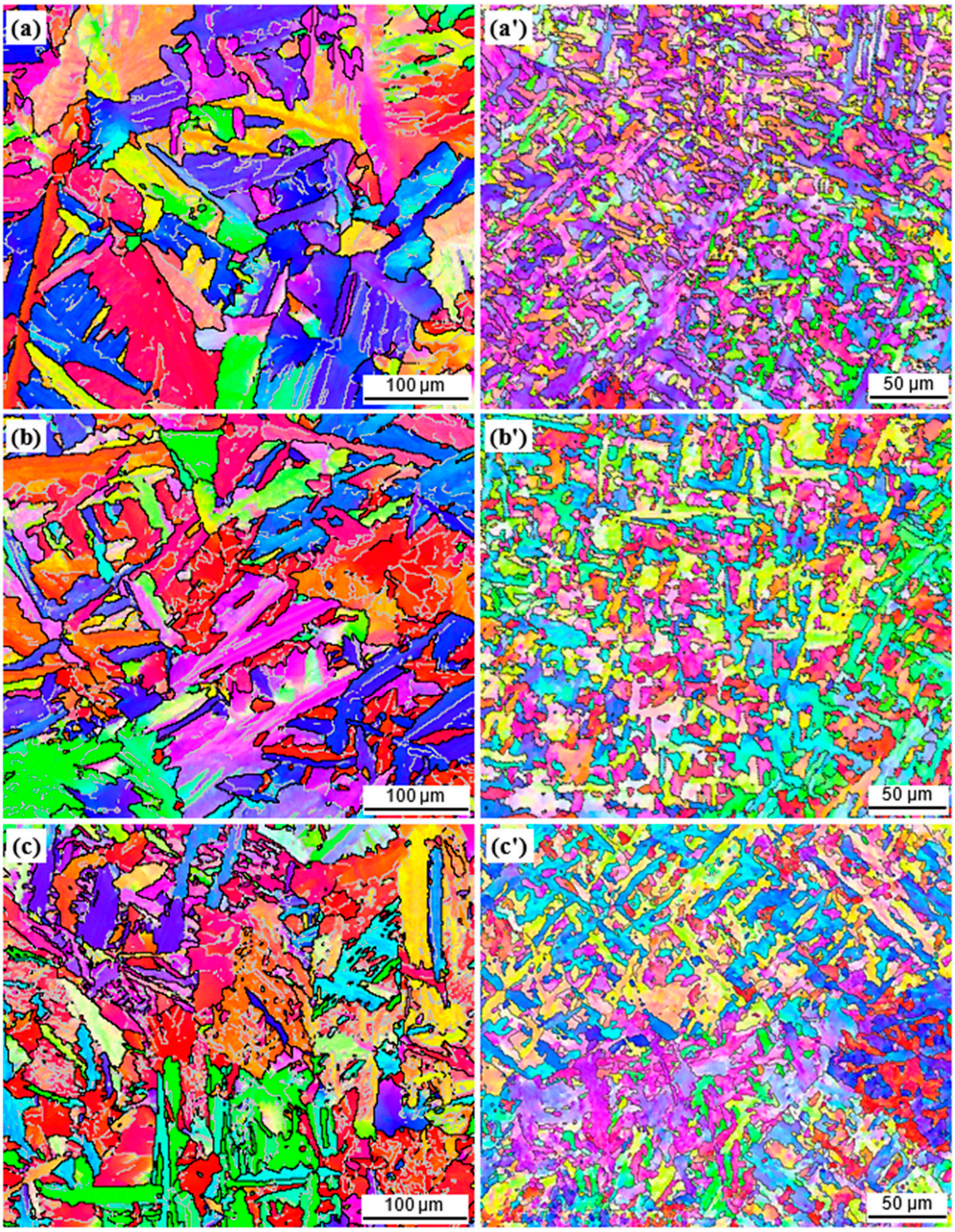

Figure 9. EBSD IPF maps of samples after LSCM thermal cycles. (**a**–**c**) are surface microstructures; (**a**′–**c**′) are interior microstructures; (**a**,**a**′), (**b**,**b**′) and (**c**,**c**′) correspond to cooling rates of 3 °C/s, 6 °C/s and 15 °C/s, respectively. The black lines indicate high-angled misorientation ≥ 15°; the grey lines indicate low-angled misorientation between 5° and 15°.

Figures 11 and 12 showed examples of the indentation shape. The Vickers hardness tester indentation was a square. In Figure 11, the micro HV indentation side length was 12.6 μm and 9.5 μm for the sample surface and interior, where the indentation depth could be calculated as 2.5 μm and 1.9 μm, respectively. In Figure 12, the macro HV indentation side length for sample surface and interior was both about 253 μm and the indentation depth was calculated to be 51 μm. The thickness of surface microstructure could be measured from the cross-section, as shown in Figure 13. The thickness of the surface layer in samples with cooling rates of 3 °C/s, 6 °C/s and 15 °C/s was 9.3 μm, 7.0 μm and 5.6 μm, respectively. It was also found that carbide tended to precipitate under the surface ferrite layer as a result of carbon diffusion inwards. In the micro HV test carried out on the sample surface, the indenter could not penetrate through the surface layer and the indentation depth was, in fact, even less than half the layer thickness. However, the macro HV indentation depth was far more than the surface layer thickness, where the indentation depth was nearly determined by the interior microstructure hardness rather than the soft surface microstructure. Therefore, the micro HV test reflected the hardness of surface microstructure and interior microstructure factually. The macro HV test reflected the sample matrix hardness for both testing positions.

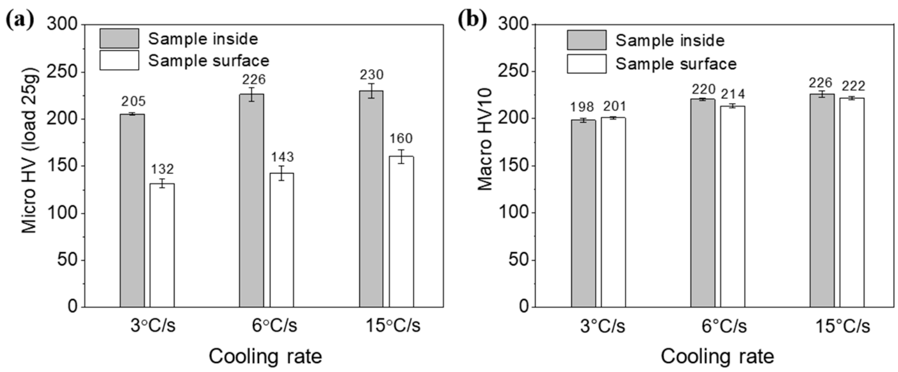

Figure 10. (**a**) Micro and (**b**) macrohardness of LSCM samples tested on the surface and inside.

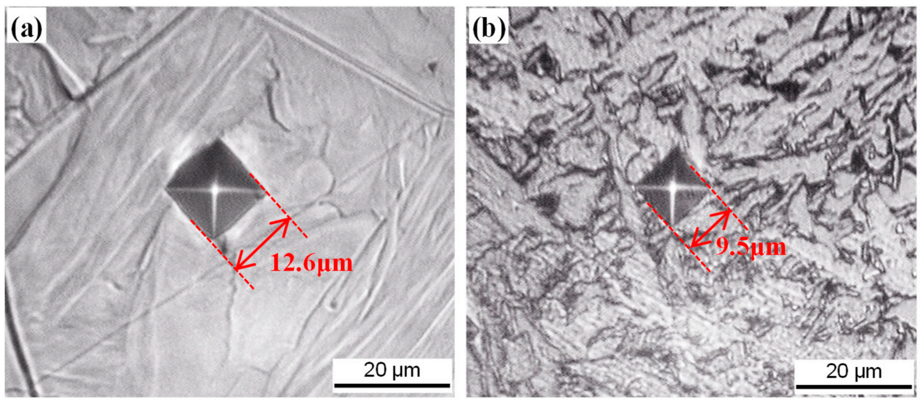

Figure 11. Microhardness indentation tested on the (**a**) surface and (**b**) inside of the LSCM sample cooled at 3 °C/s.

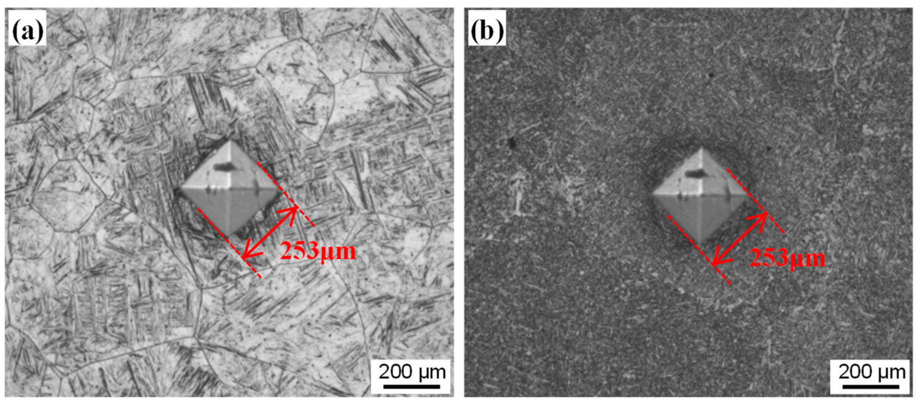

Figure 12. Macrohardness indentation tested on the (**a**) surface and (**b**) inside of the LSCM sample cooled at 3 °C/s.

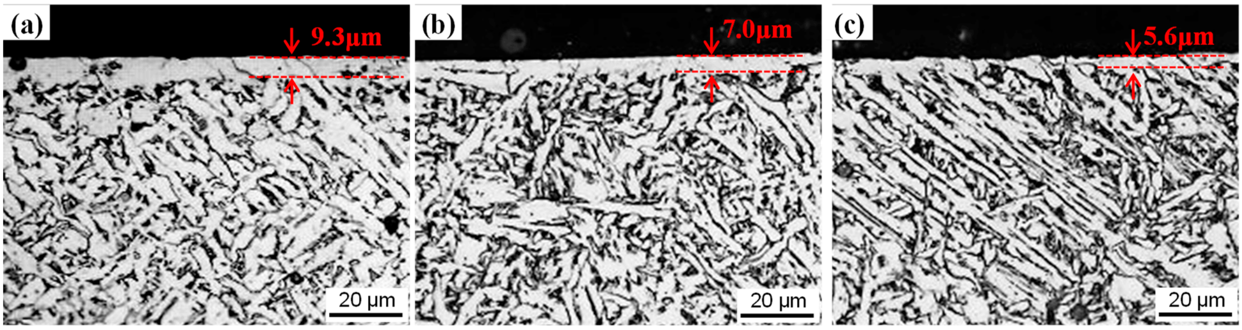

Figure 13. Optical microstructures of the LSCM sample cross-sections. (**a**–**c**) correspond to cooling rates of 3 °C/s, 6 °C/s and 15 °C/s, respectively.

The above results indicated that there exists a significant difference in morphology and hardness between the surface microstructure and actual intragranular acicular ferrite. This could bring about deviation when in situ observation was used to study AF transformation behavior. Here, a transformation-dilation experiment was carried out to further analyze the cause and degree of the discrepancy. The result was shown in Figure 14. According to the temperature-dilation curves, the sample matrix transformation intervals moved towards a lower temperature with the increase in cooling rate, which was consistent with in situ observation. However, the critical transformation points viewed by LSCM differed from those indicated by temperature-dilation curves. The start and finish transformation temperatures of surface layers revealed by LSCM were both higher than that of the sample matrix revealed by dilatometry. It was also evidently indicated in Figure 14 that for the surface microstructure, start temperatures of nucleation at grain boundaries and intragranular particles decreased with the increase in cooling rate, where the two nucleation manners happened at the same time when the cooling rate was 15 °C/s. However, according to the microstructure morphology of sample interior, the matrix transformation took place only by intragranular AF nucleation. Thus the temperature-dilation curves reflected almost pure intragranular AF transformation behavior. Additionally, the deviation of the curve from a straight line at the early stage should be partly related to the sample surface transformation.

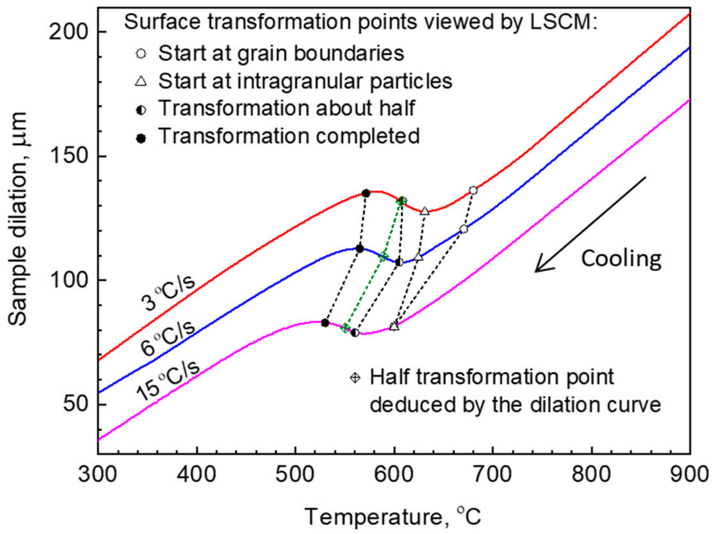

Figure 14. Cooling temperature-dilation curves by transformation equipment. Some critical points viewed by LSCM were put in the curves for comparison.

In the driving force for nucleation of a new phase, elastic strain energy $\Delta G\varepsilon$ is a component of resistance [31]. $\Delta G\varepsilon$ for sample surface layer could be negligible due to its free expansion during $\gamma \rightarrow \alpha$ transformation. Thus, the driving force for transformation of the sample surface was higher than that of the sample interior and accordingly the transformation temperature was higher for the sample surface. AF on the sample surface could only nucleate at inclusion particles located in the surface layer of several microns, which were quite limited in number. AF plates could extend along the surface or towards the interior after nucleation, where K–S orientation relationship should be kept [28,32]. For the sample interior, AF plates grew in any proper spatial directions but did not reach the sample surface because of its lower transforming temperature.

The coarse size of AF on the sample surface was due to several reasons. Firstly, AF formed at a higher temperature had a coarse size in itself, which was similar to the interior AF. Secondly, the available nucleation sites were quite limited such that hard impingement between AF plates was much weaker than that in the sample interior. In addition, ferrite plates formed via a displacive mechanism were affected by the austenite stress state. The transformation stress in austenite on the sample surface could be released largely and this contributed to a coarser AF plate size. With a coarse grain size, a lower dislocation concentration under high transformation temperature, and carbon diffusion away from the surface ferrite into the sample interior, the surface microstructure hardness was much lower than the whole AF microstructure in the same sample.

4. Conclusions

In situ observation of the transformation behavior of a Ti–Ca deoxidized low carbon steel was conducted using HT-LSCM. The microstructure between the surface and interior of the HT-LSCM sample was compared. The main conclusions are as follows:

(1) Cooling rates have significant influence on the AF transformation behavior. With an increase in cooling rate, the nucleation rate of AF increased and the surface microstructure was more interlocked. Sample surface microstructure formed at 3 °C/s was dominated by ferrite side plates, while the ferrite nucleating sites transferred from grain boundaries to intragranular particles when the cooling rate was 15 °C/s.

(2) The microstructure between the surface and interior of the HT-LSCM sample was obviously different. AF dominating microstructure was always obtained in the sample interior and was much finer than the sample surface. The micro and macrohardness values tested on the sample surface varied significantly, and the microhardness of the sample surface was much lower than that of the sample interior.

(3) The start and finish transformation temperatures of surface layers were both higher than the sample matrix. For the sample surface, the start temperatures of nucleation at grain boundaries and intragranular particles decreased with the increase in cooling rate, where the two nucleation manners happened simultaneously when the cooling rate was 15 °C/s. However, the temperature-dilation curves reflected almost pure intragranular AF transformation behavior.

(4) The combined factors led to the coarse size of AF on the sample surface. AF formed at a higher temperature resulted in a coarse size. The available particles for AF nucleation on the sample surface were quite limited, such that hard impingement between AF plates was much weaker than that in the sample interior. In addition, the transformation stress in austenite on the sample surface could be largely released, which contributed to a coarse AF plate size.

Author Contributions: Investigation, writing—original draft, X.L.; funding acquisition, methodology, writing—review and editing, G.Y.; supervision, G.W.; review and editing, R.D.K.M. All authors have read and agreed to the published version of the manuscript.

Funding: This research was funded by the National Natural Science Foundation of China (grant number U1860201).

Institutional Review Board Statement: Not applicable.

Informed Consent Statement: Not applicable.

Conflicts of Interest: The authors declare no conflict of interest.

References

1. Shim, J.H.; Cho, Y.; Chung, S.; Shim, J.D.; Lee, D. Nucleation of intragranular ferrite at Ti_2O_3 particle in low carbon steel. *Acta Mater.* **1999**, *47*, 2751–2760. [CrossRef]
2. Li, X.; Min, Y.; Liu, C.; Jiang, M. Study on the formation of intragranular acicular ferrite in a Zr–Mg–Al deoxidized low carbon steel. *Steel Res. Int.* **2016**, *86*, 622–632. [CrossRef]
3. Yuan, G.; Hu, W.; Wang, X.; Kang, J.; Zhao, J.; Di, H.; Misra, R.D.K.; Wang, G. The relationship between microstructure, crystallographic orientation, and fracture behavior in a high strength ferrous alloy. *J. Alloy. Compd.* **2017**, *695*, 526–539. [CrossRef]
4. Wang, C.; Wang, Z.D.; Wang, G.D. Effect of hot deformation and controlled cooling process on microstructures of Ti–Zr deoxidized low carbon steel. *ISIJ Int.* **2016**, *56*, 1800–1807. [CrossRef]
5. Song, F.Y.; Shi, M.H.; Wang, P.; Zhu, F.X.; Misra, R.D.K. Effect of Mn content on microstructure and mechanical properties of weld metal during high heat input welding processes. *J. Mater. Eng. Perform.* **2017**, *26*, 2947–2953. [CrossRef]
6. Jiang, M.; Wang, X.H.; Hu, Z.Y.; Wang, K.P.; Yang, C.W.; Li, S.R. Microstructure refinement and mechanical properties improvement by developing IAF on inclusions in Ti–Al complex deoxidized HSLA steel. *Mater. Charact.* **2015**, *108*, 58–67. [CrossRef]
7. Kang, Y.; Han, K.; Park, J.H.; Lee, C. Variation in the chemical driving force for intragranular nucleation in the multi-pass weld metal of Ti-containing high-strength low-alloy steel. *Metall. Mater. Trans. A.* **2015**, *46*, 3581–3591. [CrossRef]
8. Loder, D.; Michelic, S.K.; Bernhard, C. Acicular ferrite formation and its influencing factors—A review. *J. Mater. Sci. Res.* **2017**, *6*, 24–43. [CrossRef]
9. Mu, W.; Shibata, H.; Hedström, P.; Jönsson, P.G.; Nakajima, K. Ferrite formation dynamics and microstructure due to inclusion engineering in low-alloy steels by Ti_2O_3 and TiN addition. *Metall. Mater. Trans. B.* **2016**, *47*, 2133–2147. [CrossRef]
10. Wan, X.L.; Wu, K.M.; Nune, K.C.; Li, Y.; Cheng, L. In situ observation of acicular ferrite formation and grain refinement in simulated heat affected zone of high strength low alloy steel. *Sci. Technol. Weld. Joining.* **2015**, *20*, 254–263. [CrossRef]
11. Mu, W.; Shibata, H.; Hedström, P.; Jönsson, P.G.; Nakajima, K. Combination of in situ microscopy and calorimetry to study austenite decomposition in inclusion engineered steels. *Steel Res. Int.* **2016**, *87*, 10–14. [CrossRef]
12. Hanamura, T.; Shibata, H.; Waseda, Y.; Nakajima, H.; Torizuka, S.; Takanashi, T.; Nagai, K. In-situ observation of intragranular ferrite nucleation at oxide particles. *ISIJ Int.* **1999**, *39*, 1188–1193. [CrossRef]
13. Kikuchi, N.; Nabeshima, S.; Kishimoto, Y.; Matsushita, T.; Sridhar, S. Effect of Ti de-oxidation on solidification and post-solidification microstructure in low carbon high manganese steel. *ISIJ Int.* **2007**, *47*, 1255–1264. [CrossRef]
14. Kikuchi, N.; Nabeshima, S.; Kishimoto, Y.; Nakano, J.; Sridhar, S. Interface Migration Behavior of the $\delta \rightarrow \gamma$ Interface in Low Carbon High Manganese Steel Samples De-oxidized with Ti or Al. *ISIJ Int.* **2008**, *48*, 954–962. [CrossRef]
15. Kikuchi, N.; Nabeshima, S.; Yamashita, T.; Kishimoto, Y.; Sridhar, S.; Nagasaka, T. Micro-structure refinement in low carbon high manganese steels through Ti-deoxidation, characterization and effect of secondary deoxidation particles. *ISIJ Int.* **2011**, *51*, 2019–2028. [CrossRef]
16. Song, B.; Wen, B. In Situ Observation of the Evolution of Intragranular Acicular Ferrite at Mg-containing Inclusions in 16Mn Steel. *J. Manuf. Sci. Prod.* **2013**, *13*, 61–72.
17. Zhang, D.; Terasali, H.; Komizo, Y. In situ observation of the formation of intragranular acicular ferrite at non-metallic inclusions in C–Mn steel. *Acta Mater.* **2010**, *58*, 1369–1378. [CrossRef]
18. Zhou, B.W.; Li, G.Q.; Wan, X.L.; Li, Y.; Wu, K.M. In-situ observation of grain refinement in the simulated heat-affected zone of high-strength low-alloy steel by Zr-Ti combined deoxidation. *Met. Mater. Int.* **2016**, *22*, 267–275. [CrossRef]
19. Mu, W.; Jönsson, P.G.; Nakajima, K. Recent aspects on the effect of inclusion characteristics on the intragranular ferrite formation in low alloy steels: A review. *High Temp. Mater. Process.* **2017**, *36*, 309–325. [CrossRef]
20. Wang, X.; Wang, C.; Kang, J.; Yuan, G.; Misra, R.D.K.; Wang, G. An in-situ microscopy study on nucleation and growth of acicular ferrite in Ti-Ca-Zr deoxidized low-carbon steel. *Mater. Charact.* **2020**, *165*, 110381. [CrossRef]
21. Zou, X.; Sun, J.; Matsuura, H.; Wang, C. In Situ Observation of the nucleation and growth of ferrite laths in the heat-affected zone of EH36-Mg shipbuilding steel subjected to different heat inputs. *Metall. Mater. Trans. B.* **2018**, *49*, 2168–2173. [CrossRef]
22. Mu, W.; Hedström, P.; Shibata, H.; Jönsson, P.G.; Nakajima, K. High-temperature confocal laser scanning microscopy studies of ferrite formation in inclusion-engineered steels: A review. *JOM* **2018**, *70*, 2283–2295. [CrossRef]
23. Babu, S.S. The mechanism of acicular ferrite in weld deposits. *Curr. Opin. Solid State Mater. Sci.* **2004**, *8*, 267–278. [CrossRef]
24. Sarma, D.S.; Karasev, A.V.; Jönsson, P.G. On the role of non-metallic inclusions in the nucleation of acicular ferrite in steels. *ISIJ Int.* **2009**, *49*, 1063–1074. [CrossRef]
25. Byun, J.S.; Shim, J.H.; Cho, Y.W.; Lee, D.N. Non-metallic inclusion and intragranular nucleation of ferrite in Ti-killed C–Mn steel. *Acta Mater.* **2003**, *51*, 1593–1606. [CrossRef]
26. Seo, K.Y.; Kim, M.; Evans, G.M.; Kim, H.J.; Lee, C. Formation of Mn-depleted zone in Ti-containing weld metals. *Weld. World.* **2015**, *59*, 373–380. [CrossRef]
27. Wang, C.; Wang, X.; Kang, J.; Yuan, G.; Wang, G.D. Effect of thermomechanical treatment on acicular ferrite formation in Ti–Ca deoxidized low carbon steel. *Metals.* **2019**, *9*, 296. [CrossRef]
28. Enomoto, M.; Wu, K.M.; Inagawa, Y.; Murakami, T.; Nanba, S. Three-dimensional observation of ferrite plate in low carbon steel weld. *ISIJ Int.* **2005**, *45*, 756–762. [CrossRef]
29. Miyamoto, G.; Shinyoshi, T.; Yamaguchi, J.; Furuhara, T.; Maki, T.; Uemori, R. Crystallography of intragranular ferrite formed on (MnS + V(C, N)) complex precipitate in austenite. *Scr. Mater.* **2003**, *48*, 371–377. [CrossRef]

30. Kim, Y.M.; Lee, H.; Kim, N.J. Transformation behavior and microstructural characteristics of acicular ferrite in linepipe steels. *Mater. Sci. Eng. A.* **2008**, *478*, 361–370. [CrossRef]
31. Abyzov, A.S.; Fokin, V.M.; Rodrigues, A.M.; Zanotto, E.D.; Schmelzer, J.W.P. The effect of elastic stresses on the thermodynamic barrier for crystal nucleation. *J. Non-Cryst. Solids* **2016**, *432*, 325–333. [CrossRef]
32. Xiong, Z.H.; Liu, S.L.; Wang, X.M.; Shang, C.J.; Misra, R.D.K. Relationship between crystallographic structure of the Ti_2O_3/MnS complex inclusion and microstructure in the heat-affected zone (HAZ) in steel processed by oxide metallurgy route and impact toughness. *Mater. Charact.* **2015**, *106*, 232–239. [CrossRef]